INTERNATIONAL JOURNAL FOR NUMERICAL METHODS IN FLUIDS
Int. J. Numer. Meth. Fluids 2006; **51**:819–847

A framework for CFD analysis of helicopter rotors in hover and forward flight

R. Steijl[‡,¶], G. Barakos[*,†,||] and K. Badcock[§,**]

Department of Aerospace Engineering, Laboratory of Computational Fluid Dynamics,
University of Glasgow, Glasgow G12 8QQ, U.K.

SUMMARY

A framework is described and demonstrated for CFD analysis of helicopter rotors in hover and forward flight. Starting from the Navier–Stokes equations, the paper describes the periodic rotor blade motions required to trim the rotor in forward flight (blade flapping, blade lead-lag and blade pitching) as well as the required mesh deformation. Throughout, the rotor blades are assumed to be rigid and the rotor to be fully articulated with separate hinges for each blade. The employed method allows for rotors with different numbers of blades and with various rotor hub layouts to be analysed. This method is then combined with a novel grid deformation strategy which preserves the quality of multi-block structured, body-fitted grids around the blades. The coupling of the CFD method with a rotor trimming approach is also described and implemented. The complete framework is validated for hovering and forward flying rotors and comparisons are made against available experimental data. Finally, suggestions for further development are put forward. For all cases, results were in good agreement with experiments and rapid convergence has been obtained. Comparisons between the present grid deformation method and transfinite interpolation were made highlighting the advantages of the current approach. Copyright © 2006 John Wiley & Sons, Ltd.

KEY WORDS: rotorcraft CFD; hover; forward-flight; articulated rotor blades; mesh deformation

---

[*] Correspondence to: G. Barakos, Department of Engineering, University of Liverpool, Liverpool L693GH, U.K.
[†] E-mail: gbarakos@aero.gla.ac.uk
[‡] E-mail: rsteijl@eng.gla.ac.uk
[§] E-mail: gnaa36@aero.gla.ac.uk
[¶] Research Associate.
[||] Senior Lecturer.
[**] Professor.

Contract/grant sponsor: Rotorcraft aeromechanics DARP programme

Received 14 January 2005
Revised 21 July 2005
Accepted 11 August 2005

1. INTRODUCTION

The numerical simulation of flows around fixed wings has been undertaken by many authors (see Reference [1] among others) and aerodynamic loads can be obtained with relative ease at design conditions. For rotary wings, however, the situation appears to be more complicated and CFD analysis is significantly harder as documented in References [2–14]. There are several reasons contributing to this which can be grouped into two categories. First, the flow physics of a rotating wing is rich in terms of fluid mechanics phenomena. Strong vortices interacting with each other and the rotor blades, formation of a complex spiral wake behind the rotor, transition to turbulence and the wide variation of the Mach and Reynolds numbers around the azimuth are a few of the difficult issues CFD methods have to cope with. The second family of problems comes from the strong link between the aerodynamics and dynamics of the rotor blades. It is almost impossible to consider one without the other and the link between the two is the balance of forces acting on the rotor which is dictated by, and at the same time dictates the loading of the blades. The differences in blade normal velocities on the advancing and retreating sides combined with the requirement that the rotor does not produce a pitching or rolling moment on the helicopter creates the main complicating factor. The pitch and roll moments vanish for a blade incidence that depends on the azimuthal position (a smaller incidence on the advancing side and a larger one on the retreating side) and by introducing a flap hinge that gives the blades freedom to flap up and down. However, the pitch settings of the blade and the flapping deflections are not known in advance and form part of the solution. The above is commonly known as the *trimming* problem and further complicates the numerical simulations of rotors in forward flight. A detailed account of all aerodynamic challenges related to the analysis of helicopter rotors is described in the review paper of Conlisk [15].

For the above reasons, the direct CFD analysis of rotors has been undertaken by very few authors. Most of the published works focus on the numerical simulation of hovering rotors, such efforts can be found in References [6, 10–12] among others. Regarding forward-flying rotors, References [3–5, 7, 13, 14, 16, 17] document the efforts of several researchers over the last 10 years. A small number of these [4, 5, 13, 16, 17] have addressed the full problem both in terms of the aerodynamic and the aeromechanic modelling.

In the numerical simulation of a trimmed rotor in forward flight, the rotor geometry changes continuously as a result of the periodic blade motions. This requires the deformation of the CFD mesh at each time step. Forward flight simulation including the periodic motion of the blades has been undertaken by few researchers, e.g. References [7, 4, 8, 9, 16, 17] and their approaches can be split in two groups: the Chimera approach to account for the relative motion of the rotor blades [4, 7, 13] or a mesh deformation method such as the transfinite interpolation (TFI) or a spring-analogy [8, 9]. In Reference [16], a boundary conforming discontinuous Galerkin finite element approach was used with a method that adapts the mesh to the solution and also accounts for the blade motions. The time-periodicity of the flow field generated by a forward flying rotor is used in the discontinuous Galerkin approach of Reference [17]. The time-dependent flow equations are solved simultaneously in both space and time for a complete period of the problem. This allows the local grid refinement described in Reference [16] to be extended to the time dimension. In the four-dimensional space, the problem is ‘steady’.

Park and Kwon [9] used an unstructured Euler solver with spring-analogy to adjust the grid for the rotor blade motions. Sliding planes were used to couple a part of the mesh rotating with the rotor and a stationary lower part around an approximate helicopter fuselage.

The Chimera approach was used in References [7, 13] to solve the Reynolds-averaged Navier–Stokes equations on a block-structured mesh. In this approach, a separate block-structured, rigidly-moving mesh is used for each rotor blade. The blade-fixed grids are embedded in a background mesh. Along the Chimera boundaries, a tri-linear interpolation method is used for the coupling of the solution on the blade-fixed and background grids. In Reference [13], a fourth-order spatial discretization method on the background grid has been used in order to better preserve the vortex wake.

In the present work, multi-block structured meshes are used with a mesh deformation method that combines a rigid mesh motion of grid blocks attached to one of the rotor blades, and a mesh deformation method for the remaining grid blocks. This approach was designed to combine the benefits of Chimera, i.e. a high-quality grid around each of the rotor blades that does not deform, and the relatively small computational cost of TFI. The main objective of this paper is to present and validate all the extensions necessary to convert a fixed-wing CFD code to one suitable for simulating rotary wings. The structure of the paper is as follows. Section 2 presents the governing equations in an inertial frame of reference, as used in the forward flight simulations. The spatial discretization and temporal integration method are described, followed by the hovering rotor formulation for a non-inertial frame of reference. Then, the forward flight model is detailed, including the coordinate transformations used to introduce the periodic blade motions, the treatment of the periodic blade motions and the grid deformation algorithm. Subsequently, the trimming approach used in the present CFD framework for hovering and forward-flying rotors is described. Validation results are presented in Section 3 for both hovering and forward-flying rotors. In this paper, the work of Caradonna and Tung [18], the results of the HELISHAPE project [19] and the experiments of Philippe and Chattot [20] were used. Conclusions are finally drawn and suggestions for further work are put forward in Section 4.

2. BLOCK-STRUCTURED FLOW SOLVER

In this work, the helicopter-fixed frame of reference is used. The x-axis is pointing in the direction of the helicopter tail, the z-axis vertically up and the y-axis is on the advancing side of the rotor. The rotor revolves in counter-clockwise direction (seen from above). Figure 1 summarizes the notation used in this paper. A trimmed state requires that the moments generated by the rotor about the x and y axes vanish and that the rotor torque, i.e. the moment about the z-axis, is balanced by the engine torque. Furthermore, a balance of forces is required for the three coordinate directions. This state can only be achieved when the pitch of the blade changes periodically around the azimuth. The azimuth-dependent blade normal velocity and blade pitch setting give rise to a periodic flapping motion of the blade which leads to a change of the effective incidence of the blade. The periodic changes of the flow velocity over the blades (and consequently the blade drag) as well as changes of the angular moment of inertia due to the flapping motion lead to the lead-lag motion of the blade within the rotor disk plane. The rotor is assumed to be fully articulated, i.e. with a separate hinge for the

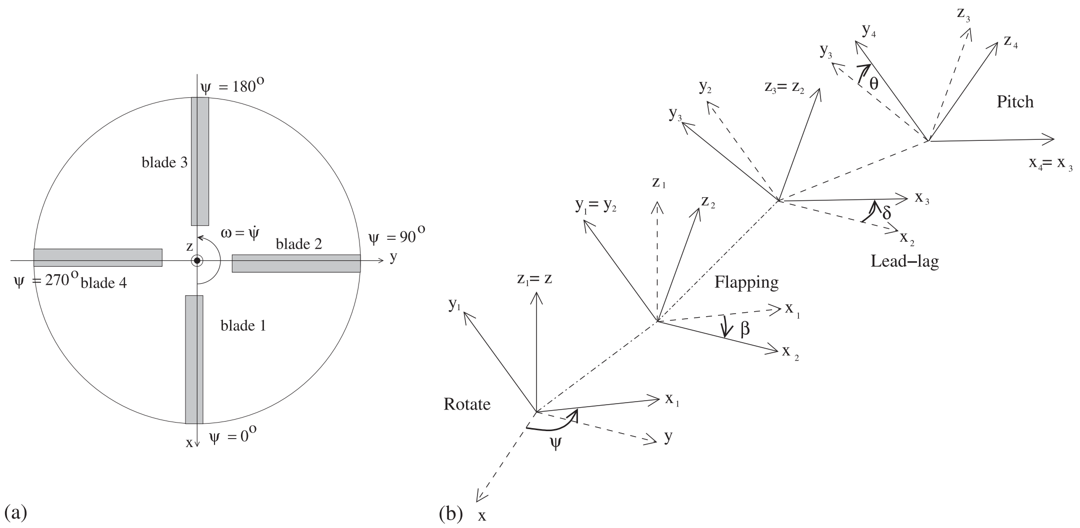

Figure 1. Definition of coordinate systems: (a) top-view of rotor disk; and (b) sketch of transformations.

three motions for each rotor blade (see Figure 1(b)). The details of the rotor construction vary for different helicopter designs. Therefore, the location and order of the hinges should be regarded as input parameters to allow rotors with different numbers of blades and with various rotor hub layouts to be analysed.

The flow solver that forms the basis of the present method is described in detail in Reference [1].

2.1. Governing equations in inertial frame of reference

The Navier–Stokes equations written in integral form in the arbitrary Lagrangian Eulerian (ALE) formulation for time-dependent domains with moving boundaries, read

$$\frac{\mathrm{d}}{\mathrm{d}t}\int_{V(t)} \vec{\mathbf{w}}\,\mathrm{d}V + \int_{\partial V(t)} (\vec{F}(\vec{\mathbf{w}}) - \vec{F}_v(\vec{\mathbf{w}}))\vec{n}\,\mathrm{d}S = \vec{S} \qquad (1)$$

The above equations form a system of conservation laws for any time-dependent control volume $V(t)$ with boundary $\partial V(t)$ and outward unit normal $\vec{n}$. The vector of conserved variables is denoted by $\vec{\mathbf{w}} = [\rho, \rho u, \rho v, \rho w, \rho E]^{\mathrm{T}}$, where ρ is the density, u, v, w are the Cartesian velocity components and E is the total internal energy per unit mass. $\vec{F}$ and $\vec{F}_v$ are the inviscid and viscous fluxes, respectively. The fluxes include the effect of the time-dependent domain, i.e. a mesh velocity is included in the contra-variant velocity components. In the absence of volume forces and in an inertial frame of reference the source term $\vec{S} = 0$. For hovering rotors, a non-inertial frame of reference is used for which $\vec{S} \neq 0$.

2.2. Spatial discretization and the dual-time stepping method

Equations (1) are discretized using a cell-centred finite volume approach on structured multi-block grids. The spatial discretization leads to a set of differential equations in time,

$$\frac{\partial}{\partial t}(\mathbf{w}_{i,j,k}V_{i,j,k}) = -\mathbf{R}_{i,j,k}(\mathbf{w}_{i,j,k}) \tag{2}$$

where $\mathbf{w}$ and $\mathbf{R}$ are the vectors of cell variables and residuals, respectively. Here, i,j,k are the cells indices in each of the grid blocks, $V_{i,j,k}$ is the cell volume. The convective terms are discretized using Osher's upwind scheme [21]. MUSCL variable interpolation is used to provide third-order accuracy and the Van Albada limiter is employed to prevent spurious oscillations near steep gradients. Boundary conditions are set using ghost cells on the exterior of the computational domain. For inviscid flow simulations, ghost values are extrapolated from the interior at solid boundaries ensuring the normal component of the velocity relative to the solid wall is zero. Similarly, for viscous flow simulations, ghost values are extrapolated at solid boundaries ensuring that the velocity takes on the solid wall velocity.

For the present time-accurate simulations, temporal integration is performed using an implicit dual-time stepping method. Following the pseudo-time formulation [22], the updated mean flow solution is calculated by solving the steady-state problems

$$\mathbf{R}^*_{i,j,k} = \frac{3V^{n+1}_{i,j,k}\mathbf{w}^{n+1}_{i,j,k} - 4V^{n}_{i,j,k}\mathbf{w}^{n}_{i,j,k} + V^{n-1}_{i,j,k}\mathbf{w}^{n-1}_{i,j,k}}{2\Delta t} + \mathbf{R}_{i,j,k}\left(\mathbf{w}^{n+1}_{i,j,k}\right) = 0 \tag{3}$$

where the terms $V^{n-1}_{i,j,k}$, $V^{n}_{i,j,k}$ and $V^{n+1}_{i,j,k}$ represent the cell volume at different (real) time steps. Equation (3) represents a nonlinear system of equations. This system can be solved by introducing an iteration through *pseudo-time* τ to the steady state, as given by

$$\underbrace{V^{n+1}_{i,j,k}\frac{\mathbf{w}^{n+1,m+1}_{i,j,k} - \mathbf{w}^{n+1,m}_{i,j,k}}{V^{n+1}_{i,j,k}\Delta\tau}}_{\mathrm{A}} + \frac{3V^{n+1}_{i,j,k}\mathbf{w}^{n+1,m}_{i,j,k} - 4V^{n}_{i,j,k}\mathbf{w}^{n}_{i,j,k} + V^{n-1}_{i,j,k}\mathbf{w}^{n-1}_{i,j,k}}{2V^{n+1}_{i,j,k}\Delta t} + \frac{\mathbf{R}_{i,j,k}\left(\mathbf{w}^{n+1,m}_{i,j,k}\right)}{V^{n+1}_{i,j,k}} = 0 \tag{4}$$

where the mth pseudo-time iterate at real time step $n+1$ is denoted by $\mathbf{w}^{n+1,m}$ and the cell volumes are constant during the pseudo-time iteration. The unknown $\mathbf{w}^{n+1}_{i,j,k}$ is obtained when term A in Equation (4) converges to a specified tolerance. An implicit scheme is used for the pseudo-time integration. In the implicit integration method, the flux residual $\mathbf{R}_{i,j,k}(\mathbf{w}^{n+1}_{i,j,k})$ is linearized as

$$\begin{aligned}\mathbf{R}_{i,j,k}(\mathbf{w}^{n+1}) &= \mathbf{R}_{i,j,k}(\mathbf{w}^{n}_{i,j,k}) + \frac{\partial \mathbf{R}_{i,j,k}(\mathbf{w}^{n}_{i,j,k})}{\partial t}\Delta t + O(\Delta t^2)\\ &\approx \mathbf{R}^{n}_{i,j,k}(\mathbf{w}^{n}_{i,j,k}) + \frac{\partial \mathbf{R}^{n}_{i,j,k}}{\partial \mathbf{w}^{n}_{i,j,k}}(\mathbf{w}^{n+1}_{i,j,k} - \mathbf{w}^{n}_{i,j,k})\end{aligned} \tag{5}$$

Equation (4) then becomes a system of linear equations which is solved using the generalized conjugate gradient method [23] with a block incomplete lower–upper (BILU) pre-conditioner. Typically the pseudo-time integration in Equation (4) is continued at each real time step until the residual has dropped three orders of magnitude. For the simulations presented here, this typically required 25–35 pseudo-time steps.

2.3. Hover formulation

Assuming that the wake shed from the rotor is steady, the flow around a hovering rotor can be treated as a steady-state problem. Furthermore, the periodicity of the flow in the azimuthal direction can be used to reduce the computational expense, i.e. for an n-bladed rotor a $1/n$ segment of the complete domain with periodic boundary conditions suffices to model the rotor.

The present hover models assumes a constant rotation rate ω about the x-, y- or z-axis. If rotation about the z-axis is assumed the rotation vector becomes $\vec{\omega} = (0, 0, \omega)^{\mathrm{T}}$. The hover model uses a mesh that does not rotate about the z-axis. A non-inertial frame of reference is used to account for the rotor rotation, as introduced in Reference [10]. The centripetal and Coriolis acceleration terms in the momentum equations are modelled here using a combination of a mesh velocity in the ALE formulation of the Navier–Stokes equations (1) and a source term for the momentum equations.

The mesh velocity introduced in the system of equations (1) corresponds to mesh rotation in the direction of the rotor, i.e. a reference velocity $\vec{u}_{\mathrm{ref}} = \omega \times \vec{r}$ is introduced, where $\vec{r}$ is the position vector of a cell.

In addition to the mesh velocity, a source term for the momentum equations is introduced:

$$\vec{S} = [0, -\rho\omega \times \vec{u}_h, 0]^{\mathrm{T}} \tag{6}$$

where $\vec{u}_h$ is the velocity field in the present rotor-fixed frame of reference.

The non-inertial frame of reference used here has two benefits over a rotating frame of reference: (i) the energy equation is unchanged by the rotation vector $\vec{\omega}$ and (ii) a vanishing ‘undisturbed’ velocity field occurs in contrast to the position-dependent ‘undisturbed’ velocity field in the rotating frame of reference, which is given by $-\omega \times \vec{r}$. This is beneficial in imposing boundary conditions. Two types of far-field boundary conditions are used. The first is based on imposing unperturbed free-stream/linear extrapolation at the far-field of the computational domain. Extrapolation is used in the vertical direction on the inflow and outflow boundaries. Experience shows that the far-field boundaries need to be at least 5 rotor radii away from the rotor if far-field boundary conditions are used. Moving the far-field boundary closer to the rotor leads to significant flow re-circulation within the domain. The second approach is a ‘potential sink/Froude’ boundary condition and is designed to suppress re-circulation. In this case, a potential sink is placed at the rotor origin [2, 6, 11] and based on actuator-disk theory, a constant axial (outflow) velocity is prescribed on a circular part of the outflow boundary face. The magnitude of this velocity is determined by the rotor thrust and the outflow radius by the following empirical relation [2]:

$$\frac{R_{\mathrm{outflow}}}{R} = 0.78 + 0.22\ \exp(-d_{\mathrm{outflow}}/R) \tag{7}$$

Actuator-disk theory predicts a wake contraction to $R/\sqrt{2}$ far from the disk, where the axial velocity is twice the induced axial velocity through the rotor disk. In this work, $d_{\mathrm{outflow}}/R \approx 4$ and $R_{\mathrm{outflow}}/R \approx 0.783$ are used. On the remainder of the far-field boundary, the velocity due to the potential sink is imposed. The strength of the sink is chosen to balance the mass flow into and out of the computational domain.

2.4. *Forward flight modelling*

The construction of rotor heads is fully explained in many text books, e.g. References [24–27]. For a typical helicopter rotor, the rotor blades are attached to the rotor head by a set of three hinges: the flap hinge allows the blade to flap up and down, the lead-lag hinge allows the blade an in-plane forward or backward motion and the feathering hinge is used to change the blade pitch. In a number of modern helicopters, one or more of these hinges is replaced by a flexible connecting beam. The control input consists of a 'collective' pitch, i.e. a revolution-averaged pitch that is identical for all blades, and a 'cyclic' pitch, i.e. a periodic pitch change in the azimuthal direction. The deflections in flapping and lead-lag result from balances of inertial and aerodynamic forces. In hover, the blade encounters a constant blade normal velocity, and as a result, no cyclic pitch change is needed. In this case, a collective pitch is set and a constant flapping deflection ('coning') results. The blade tips trace out a plane called the *tip-path plane*, which is horizontal for hovering rotors.

In forward flight, the blades experience a blade normal velocity which depends on the azimuthal position. For a radial station r/R of a rotor blade, the blade normal Mach number is

$$M_n(\psi) = M_{\text{tip}}\frac{r}{R} + M_\infty \sin\psi = M_{\text{tip}}\left(\frac{r}{R} + \mu\sin\psi\right)$$

where $\mu = M_\infty/M_{\text{tip}}$ is the *advance ratio* of the rotor.

Level forward flight of a helicopter requires that the rotor is trimmed. Assuming that the rotor creates forces normal to the tip-path plane, this plane is tilted forward to generate the necessary forward thrust. A level forward flight of a helicopter involves the following unknowns: the forward tilt of the tip-path plane, the collective pitch, cyclic pitch and flapping and lead-lag harmonics. Obtaining these is part of the *trimming problem*. Considering the above, a forward flight model in a CFD method should involve: (i) a method to change the 'collective' blade pitch, and to introduce the periodic 'cyclic' pitch and periodic flapping and lead-lag deflections, (ii) a method to adjust the mesh to account for the changing blade pitch and deflections and (iii) a trimming method to determine the collective pitch, cyclic pitch and flapping and lead-lag harmonics.

2.5. *Formulation of rotor blade motion*

Figure 1(a) shows a top-view of a rotor in forward flight. The azimuthal angle $\psi = 0°$ corresponds to a position on the positive x-axis and $\psi = 90°$ to the positive y-axis. The blades are numbered anti-clockwise, starting with blade one that is aligned with the x-axis at $\psi = 0°$. Furthermore, the following assumptions are made: the rotor blades are rigid and connected to the rotor hub by a set of three hinges: flap hinge, lead-lag hinge and pitch centre. The order of the hinges can be different, though for the rest of the discussion we will continue with the order shown in Figure 1(b). The same figure, also shows the relationship between the helicopter-fixed and blade-fixed frames of reference. The following notation is used:

1. $\mathbf{x}$: the helicopter-fixed frame of reference.
2. $\mathbf{x}^{(1)}$: the blade frame of reference after applying rotation.
3. $\mathbf{x}^{(2)}$: the blade frame of reference after applying rotation and flapping.

4. $\mathbf{x}^{(3)}$: the blade frame of reference after applying rotation, flapping and lead-lag.
5. $\mathbf{x}^{(4)}$: the blade frame of reference after applying rotation, flapping, lead-lag and pitch.

The rotation, flapping, lead-lag and pitch angles are defined as

$$\begin{aligned}
\psi &= \omega t \\
\beta(\psi) &= \beta_0 - \beta_{1s}\sin(\psi) - \beta_{1c}\cos(\psi) - \beta_{2s}\sin(2\psi) - \beta_{2c}\cos(2\psi) - \cdots \\
\delta(\psi) &= \delta_0 - \delta_{1s}\sin(\psi) - \delta_{1c}\cos(\psi) - \delta_{2s}\sin(2\psi) - \delta_{2c}\cos(2\psi) - \cdots \\
\theta(\psi) &= \theta_0 - \theta_{1s}\sin(\psi) - \theta_{1c}\cos(\psi) - \theta_{2s}\sin(2\psi) - \theta_{2c}\cos(2\psi) - \cdots
\end{aligned} \tag{8}$$

where ω is the constant rate of rotation about the z-axis. The collective pitch is θ_0 and the coning angle is β_0. In the present work, only the first harmonic terms in Equation (8) are considered though inclusion of higher harmonics is trivial. The following transformation matrices are introduced for rotation (about the z-axis), flapping (about the $y^{(1)}$-axis), lead-lag (about the $z^{(2)}$-axis) and pitch (about the $x^{(3)}$-axis):

$$\begin{aligned}
C_{\text{rot}} &= \begin{pmatrix} \cos\psi & -\sin\psi & 0 \\ \sin\psi & \cos\psi & 0 \\ 0 & 0 & 1 \end{pmatrix}, \quad
C_{\text{flap}} = \begin{pmatrix} \cos\beta & 0 & -\sin\beta \\ 0 & 1 & 0 \\ \sin\beta & 0 & \cos\beta \end{pmatrix} \\
C_{\text{lag}} &= \begin{pmatrix} \cos\delta & -\sin\delta & 0 \\ \sin\delta & \cos\delta & 0 \\ 0 & 0 & 1 \end{pmatrix}, \quad
C_{\text{pitch}} = \begin{pmatrix} 1 & 0 & 0 \\ 0 & \cos\theta & -\sin\theta \\ 0 & \sin\theta & \cos\theta \end{pmatrix}
\end{aligned} \tag{9}$$

and the corresponding time derivatives are

$$\begin{aligned}
\frac{\mathrm{d}C_{\text{rot}}}{\mathrm{d}t} &= \omega \begin{pmatrix} -\sin\psi & -\cos\psi & 0 \\ \cos\psi & -\sin\omega & 0 \\ 0 & 0 & 0 \end{pmatrix}, \quad
\frac{\mathrm{d}C_{\text{flap}}}{\mathrm{d}t} = \dot{\beta} \begin{pmatrix} -\sin\beta & 0 & -\cos\beta \\ 0 & 0 & 0 \\ \cos\beta & 0 & -\sin\beta \end{pmatrix} \\
\frac{\mathrm{d}C_{\text{lag}}}{\mathrm{d}t} &= \dot{\delta} \begin{pmatrix} -\sin\delta & -\cos\delta & 0 \\ \cos\delta & -\sin\delta & 0 \\ 0 & 0 & 0 \end{pmatrix}, \quad
\frac{\mathrm{d}C_{\text{pitch}}}{\mathrm{d}t} = \dot{\theta} \begin{pmatrix} 0 & 0 & 0 \\ 0 & -\sin\theta & -\cos\theta \\ 0 & \cos\theta & -\sin\theta \end{pmatrix}
\end{aligned} \tag{10}$$

Assuming constant rotation rate, the temporal derivatives of the flap, lead-lag and pitch angles can be written as

$$\frac{\mathrm{d}\beta}{\mathrm{d}t} = \omega\frac{\mathrm{d}\beta}{\mathrm{d}\psi}, \quad \frac{\mathrm{d}\delta}{\mathrm{d}t} = \omega\frac{\mathrm{d}\delta}{\mathrm{d}\psi}, \quad \frac{\mathrm{d}\theta}{\mathrm{d}t} = \omega\frac{\mathrm{d}\theta}{\mathrm{d}\psi} \tag{11}$$

The coordinates of a point P in the blade-fixed system in terms of its co-ordinates in the helicopter-fixed frame of reference, after rotation (ψ), flapping (β), lead-lag (δ) and pitching (θ) become:

$$\begin{aligned}\vec{x}_P &= C_{\text{rot}}C_{\text{flap}}C_{\text{lag}}C_{\text{pitch}}(\vec{x}_P-\vec{x}_{\text{pitch}})+C_{\text{rot}}C_{\text{flap}}C_{\text{lag}}(\vec{x}_{\text{pitch}}-\vec{x}_{\text{lag}})\\ &\quad +C_{\text{rot}}C_{\text{flap}}(\vec{x}_{\text{lag}}-\vec{x}_{\text{flap}})+C_{\text{rot}}\vec{x}_{\text{flap}}\end{aligned}\tag{12}$$

where $\vec{x}_{\text{flap}}$, $\vec{x}_{\text{lag}}$ and $\vec{x}_{\text{pitch}}$ define the locations of the flap hinge, lead-lag hinge and the pitch centre. The velocity of P in terms of the helicopter-fixed frame of reference is then

$$\begin{aligned}\frac{\mathrm{d}\vec{x}_P}{\mathrm{d}t} &= \underbrace{\frac{\mathrm{d}C_{\text{rot}}C_{\text{flap}}C_{\text{lag}}C_{\text{pitch}}}{\mathrm{d}t}(\vec{x}_P-\vec{x}_{\text{pitch}})}_{\text{I}}+\underbrace{\frac{\mathrm{d}C_{\text{rot}}C_{\text{flap}}C_{\text{lag}}}{\mathrm{d}t}(\vec{x}_{\text{pitch}}-\vec{x}_{\text{lag}})}_{\text{II}}\\ &\quad +\underbrace{\frac{\mathrm{d}C_{\text{rot}}C_{\text{flap}}}{\mathrm{d}t}(\vec{x}_{\text{lag}}-\vec{x}_{\text{flap}})}_{\text{III}}+\underbrace{\frac{\mathrm{d}C_{\text{rot}}}{\mathrm{d}t}\vec{x}_{\text{flap}}}_{\text{IV}}\end{aligned}\tag{13}$$

The terms in Equation (13) represent the following contributions:

- Term I is the contribution due to the combined rotation, flapping, lead-lag and pitching motion relative to the pitch centre.
- Terms II, III and IV together represent the contribution due to the movement of the pitch centre as a result of the rotation, flapping and lead-lag motion, which can be written as

$$\begin{aligned}&\frac{\mathrm{d}C_{\text{rot}}}{\mathrm{d}t}[\vec{x}_{\text{flap}}+C_{\text{flap}}(\vec{x}_{\text{lag}}-\vec{x}_{\text{flap}})+C_{\text{flap}}C_{\text{lag}}(\vec{x}_{\text{pitch}}-\vec{x}_{\text{lag}})]\quad\text{(rotation)}\\ &+C_{\text{rot}}\frac{\mathrm{d}C_{\text{flap}}}{\mathrm{d}t}[(\vec{x}_{\text{lag}}-\vec{x}_{\text{flap}})+C_{\text{lag}}(\vec{x}_{\text{pitch}}-\vec{x}_{\text{lag}})]\quad\text{(flapping)}\\ &+C_{\text{rot}}C_{\text{flap}}\frac{\mathrm{d}C_{\text{lag}}}{\mathrm{d}t}(\vec{x}_{\text{pitch}}-\vec{x}_{\text{lag}})\quad\text{(lead-lag)}\end{aligned}$$

The derivatives of the matrix products in Equation (13) are computed using the recurrence relations:

$$\begin{aligned}\frac{\mathrm{d}C_{\text{rot}}C_{\text{flap}}}{\mathrm{d}t} &= C_{\text{rot}}\frac{\mathrm{d}C_{\text{flap}}}{\mathrm{d}t}+\frac{\mathrm{d}C_{\text{rot}}}{\mathrm{d}t}C_{\text{flap}}\\ \frac{\mathrm{d}C_{\text{rot}}C_{\text{flap}}C_{\text{lag}}}{\mathrm{d}t} &= (C_{\text{rot}}C_{\text{flap}})\frac{\mathrm{d}C_{\text{lag}}}{\mathrm{d}t}+\frac{\mathrm{d}(C_{\text{rot}}C_{\text{flap}})}{\mathrm{d}t}C_{\text{lag}}\\ \frac{\mathrm{d}C_{\text{rot}}C_{\text{flap}}C_{\text{lag}}C_{\text{pitch}}}{\mathrm{d}t} &= (C_{\text{rot}}C_{\text{flap}}C_{\text{lag}})\frac{\mathrm{d}C_{\text{pitch}}}{\mathrm{d}t}+\frac{\mathrm{d}(C_{\text{rot}}C_{\text{flap}}C_{\text{lag}})}{\mathrm{d}t}C_{\text{pitch}}\end{aligned}$$

Using Equations (8) and (11)–(13), the position and velocity of any point P in the helicopter-fixed frame of reference can be expressed as functions of the azimuth ψ.

2.6. Mesh movement, deformation and multi-block topology

For forward-flight simulations, a technique was developed to account for periodic rotor blade motions using deforming block-structured meshes. The method aims to maintain the grid quality as the mesh is deformed at each time-step. The present approach divides the multi-block mesh in two types of grid blocks: blocks moving 'rigidly' with one of the rotor blades and blocks that are deformed to account for the motion of the blade. This approach preserves the quality of the mesh near the blades and moves the deformation of the mesh to less critical areas of the computational domain. The method imposes constraints on the employed multi-block topology and a sensible choice of the size of the blade-attached mesh blocks is needed to prevent large mesh deformations near the block boundaries of the blade-attached blocks. The block selection process is shown in Figure 2 for one quarter of the computational domain of the four-bladed ONERA 7A model rotor [19]. A C–H block topology is used for the grid around the rotor blades. The blocking uses extruded blocks from the rotor blade tip towards the far-field boundary and from the rotor root to the rotor hub, i.e. the grid is not collapsed around the blade tips. The helicopter rotors considered here have a generic rotor hub structure. The present method requires a radial block division between the rotor hub and the root of the blades. Another radial block division is needed some distance outboard (typically one chord length) of the blade tips.

The block selection method involves the following steps:

1. Blocks connected to a rotor blade are tagged to move 'rigidly'. For each of these blade-attached blocks, the blade number is stored.
2. For the remaining blocks, the connections to 'rigid' moving blocks are determined. If a block has two connections to blade-attached blocks moving with the same rotor blade, the block is tagged to move 'rigidly' with that blade. This creates a layer of blocks around the rotor blades with a smooth bounding surface, i.e. without 'gaps' near the edges. An example of this bounding surface is shown as shaded surfaces in Figures 2(c) and (d).
3. For the blocks tagged to move 'rigidly', the grid in the initial position ($\psi = 0^\circ$) and without blade articulation is stored for reference.

Using this 'reference' grid, Equation (12) can now be used to update the grid from time level n to $n+1$ for the blocks tagged for rigid-mesh motion.

$$\mathbf{x}^{t=n+1} = C_{\text{rot}} C_{\text{flap}} C_{\text{lag}} C_{\text{pitch}} (\mathbf{x}^{\text{reference}} - \vec{x}_{\text{pitch}}) + C_{\text{rot}} C_{\text{flap}} C_{\text{lag}} (\vec{x}_{\text{pitch}} - \vec{x}_{\text{lag}}) + C_{\text{rot}} C_{\text{flap}} (\vec{x}_{\text{lag}} - \vec{x}_{\text{flap}}) + C_{\text{rot}} \vec{x}_{\text{flap}} \tag{14}$$

where C_{rot}, C_{flap}, C_{lag} and C_{pitch} are determined for the azimuth at time level $n+1$. The grid velocity needed for time-accurate computations is determined for the 'rigidly' moving blocks using Equation (13):

$$\frac{\mathrm{d}\mathbf{x}^{n+1}}{\mathrm{d}t} = \frac{\mathrm{d}C_{\text{rot}} C_{\text{flap}} C_{\text{lag}} C_{\text{pitch}}}{\mathrm{d}t} (\mathbf{x}^{\text{reference}} - \vec{x}_{\text{pitch}}) + \frac{\mathrm{d}C_{\text{rot}} C_{\text{flap}} C_{\text{lag}}}{\mathrm{d}t} (\vec{x}_{\text{pitch}} - \vec{x}_{\text{lag}}) + \frac{\mathrm{d}C_{\text{rot}} C_{\text{flap}}}{\mathrm{d}t} (\vec{x}_{\text{lag}} - \vec{x}_{\text{flap}}) + \frac{\mathrm{d}C_{\text{rot}}}{\mathrm{d}t} \vec{x}_{\text{flap}} \tag{15}$$

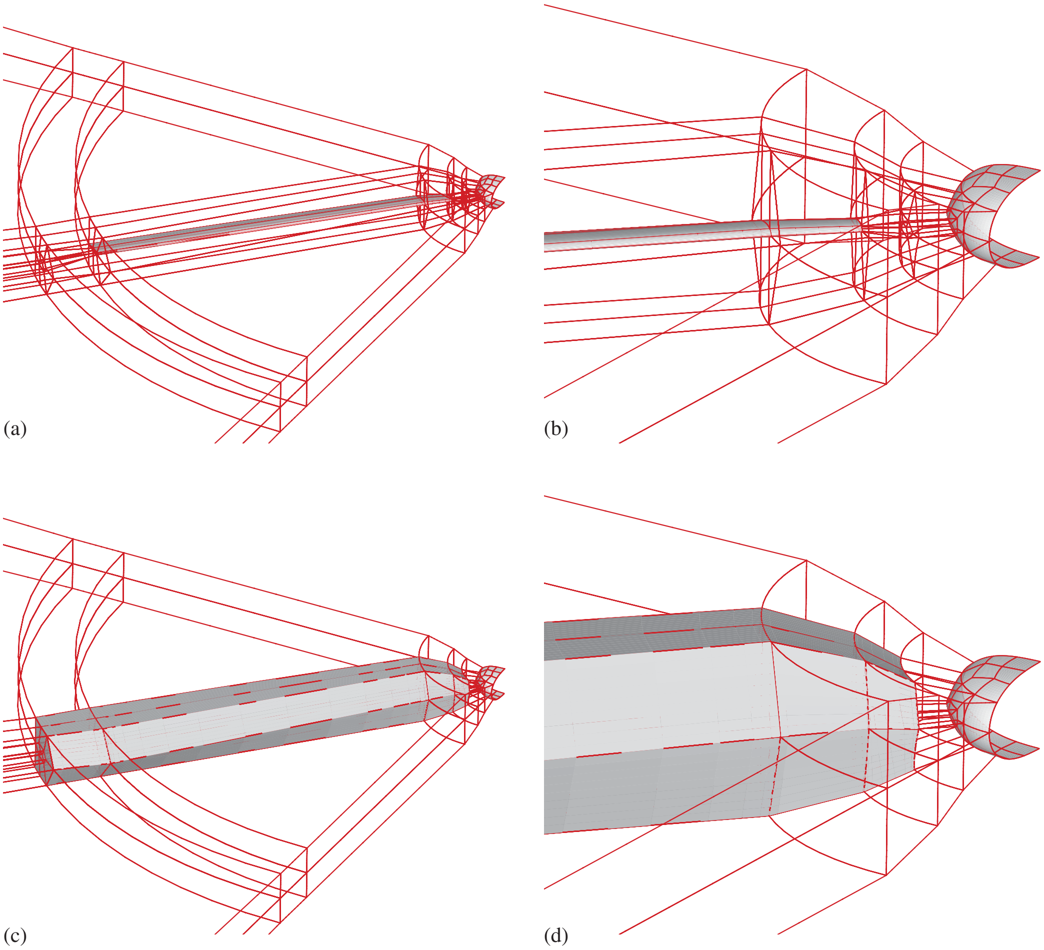

Figure 2. Blocking for the four-bladed ONERA 7A rotor: (a) C–H blocking around the blade; (b) treatment of the hub region; (c) ‘Rigid’ part of mesh around the blade; and (d) ‘Rigid’ mesh in hub region.

The method for updating the grid for the blocks not moving with one of the rotor blades involves the following steps:

1. Block faces connected to ‘rigidly’ moving blocks are selected.
2. These block faces are treated as rigid, using Equation (14).
3. The effect of rotation is subtracted from the mesh updates at this stage.
4. The mesh updates of block faces connected to ‘rigidly’ moving blocks form the input to the TFI method used for the deforming blocks.
5. After applying the TFI method, the deformed mesh is rotated to the new azimuth.

The grid velocity for the blocks not moving with one of the rotor blades is obtained using similar steps as for the mesh deformation, i.e. the block faces, connected to 'rigidly' moving blocks are selected and for these faces, Equation (13) gives the grid velocity. Then, the effect of the rotor rotation is subtracted. The remaining grid velocity is due to the periodic blade motion and is computed from the grid velocity at the block face(s) using the TFI method. Finally, the effect of the mesh rotation is added.

For a two-bladed rotor, Figure 3 presents a comparison between a baseline grid and deformed grids for 8° pitch increase, 5° flapping deflection and 2° lead-lag deflection (conditions representative of the retreating side of rotor disks). The grid obtained using the present method is compared with the grid resulted from applying TFI at all blocks. Details of the meshes are shown for the outboard station $r/R \approx 0.8$ and the near-hub region. Figure 3 clearly shows the large distortion of the grid in the vicinity of the blade leading-edge due to the pitch change for the case the TFI method is used. An appropriate choice of the dimensions of the blade-attached blocks is needed for large pitch changes and/or flapping and lead-lag deflections. For the results in Figure 3, one chord length was used as distance along the directions normal to the blade and normal to the blade tip. The maximum relative cell volume change is shown in Table I for an example involving the ONERA 7A model rotor [19]. The table compares the two mesh-deformation methods for several values of the changes in flapping deflection (β) and blade pitch (θ). The values of $\delta\beta$ and $\delta\theta$ are representative for the changes occurring within a revolution of the rotor in forward flight. Although the maximum relative cell volume change is just one indicator of mesh quality, Table I does show that moving the mesh blocks rigidly with the rotor blade results in changes that are about an order of magnitude smaller than if TFI is applied throughout the domain. With the proposed method, mesh deformation only occurs in blocks not connected to either of the blades, i.e. in blocks where mesh cells are typically much larger than those close to the blades.

2.7. *Trimming method*

The trimming method used here is based on blade-element theory, which enables the solution of approximate equations for the aero-mechanics of the rotor. The trimming method consists of an initial trim-state computation and a number of subsequent re-trimming steps. The initial trim state can be obtained either off-line or within the CFD solver. Due to the simple nature of the aerodynamic model, the initial trim-state cannot be expected to be very accurate, however, during re-trimming steps, blade loads computed using the CFD solution are used. During re-trimming, the collective pitch is updated via a Newton–Raphson process, where the simple aerodynamic model is only used to compute the derivatives of the loads. As a result, upon convergence, the trim state is independent of the approximate aerodynamics. For simulations of trimmed hovering rotors, the re-trimming is carried out after the steady flow solution has converged to a prescribed level. Re-trimming is repeated every n_{retrim} steps (250 in the present work). For simulations of forward-flying rotors, re-trimming is carried out after completion of about 3 rotor revolutions using revolution-averaged integrated loads from the CFD solution. The trimming method needs a target thrust coefficient c_{T} as input. In addition, models for the fuselage and its drag are necessary in order to compute the total drag, as a function of the helicopter's advance ratio. From the rotor thrust and total drag, the orientation of the *tip-path plane* can be obtained, i.e. the forward tilt. For a rotor at straight level flight conditions the orientation of the tip-path plane can be obtained from $\theta_{\text{tpp}} = -D/W$, where D and W represent

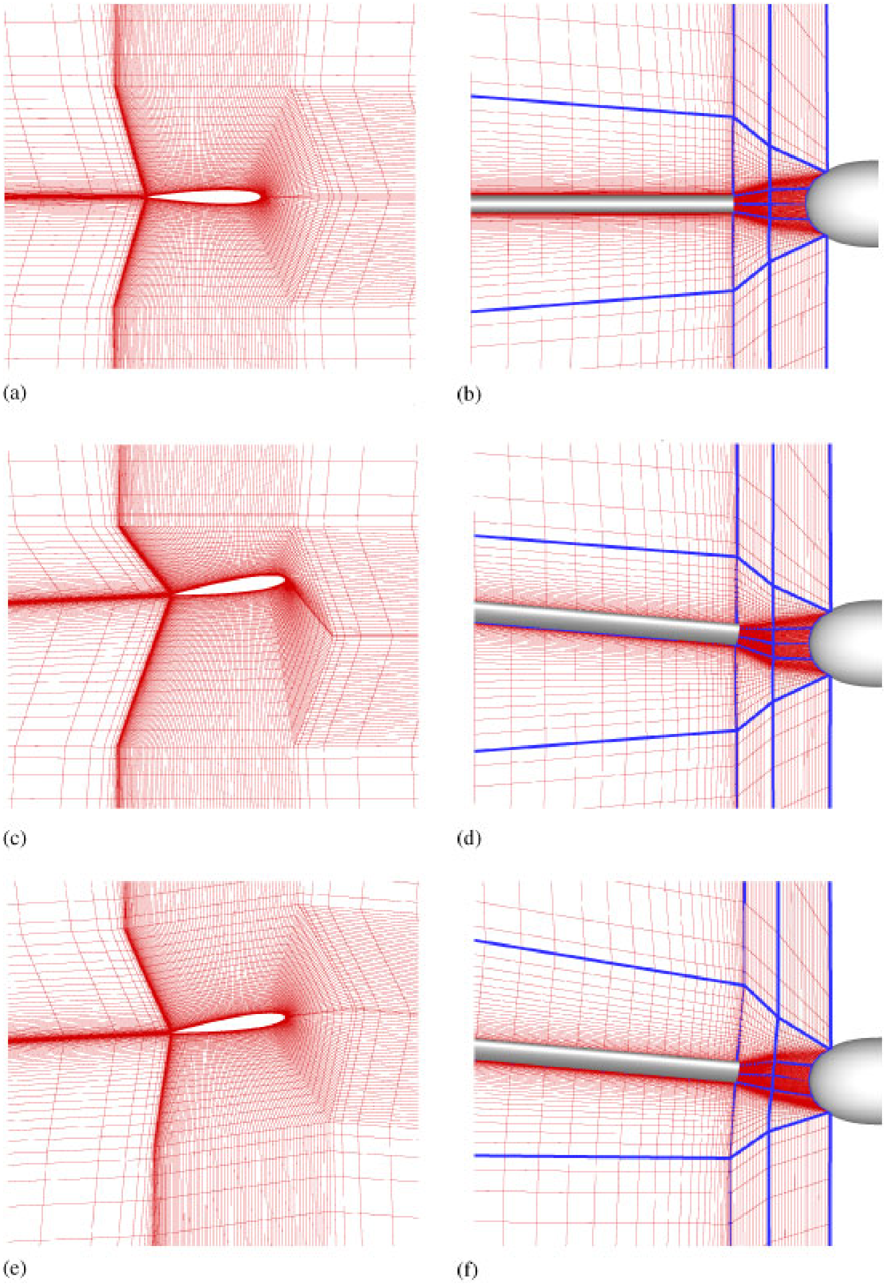

Figure 3. (a, b) Original, (c, d) deformed grid using the TFI method and (e, f) deformed grid using the proposed mesh motion/deformation method. The mesh at a radial station of $r/R = 0.80$ (a, c, e) and the mesh in the near-hub region (b, d, f). For all cases, 8° pitch change, 5° flapping deflection and 2° lead-lag deflection were applied: (a) outboard, baseline grid; (b) hub, baseline grid; (c) outboard, deformed (TFI); (d) hub, deformed (TFI); (e) outboard, deformed (present method); and (f) hub, deformed (present method).

Table I. Maximum relative cell volume change for the articulated ONERA 7A rotor.

$\delta\beta$	2.0°	2.0°	3.0°	3.0°	2.0°	2.0°	3.0°	3.0°
$\delta\theta$	5.0°	−5.0°	5.0°	−5.0°	3.0°	−3.0°	3.0°	−3.0°
TFI	0.6993	0.6588	1.0079	0.9547	0.6772	0.6302	0.9908	0.9261
Rigid/TFI	−0.1199	−0.1142	−0.1399	−0.1185	0.0886	−0.0698	0.1077	−0.0736

A collective of 7.5° and a coning of 0.0° were built in the CFD grid.

the total drag of the helicopter and its weight. Here, θ_{tpp} is assumed to be small and is taken positive for backward tilt. The aerodynamic model needs an estimate of the induced velocity in the tip-path plane. The induced velocity is assumed constant in the tip-path plane, and is obtained from Glauert's propeller theory (see References [24–26]). The non-dimensional inflow factor λ is defined as

$$\lambda = \frac{V \sin \theta_{\text{tpp}+v_i}}{\Omega R} = \mu\theta_{\text{tpp}} + \lambda_i \tag{16}$$

where v_i is the induced velocity (<0 for a lifting rotor) and $V \sin \theta_{\text{tpp}}$ the inflow due to the rotor disk tilt. In Equation (16), R is the rotor radius and Ω the rotation rate. The inflow factor λ is computed using a Newton–Raphson method to solve the following non-linear equation for λ_i:

$$\lambda_i = -\frac{c_{\text{T}}}{2} \frac{1}{\sqrt{\mu^2 + (\mu \sin \theta_{\text{tpp}} + \lambda_i)^2}} \tag{17}$$

where the thrust coefficient c_{T} is defined as

$$c_{\text{T}} = \frac{W}{\rho A (\Omega R)^2} \tag{18}$$

From classical theory [24–26], the collective pitch, cyclic pitch and flapping coefficients can then be calculated. For the collective pitch, the following expression is used:

$$\frac{c_{\text{T}}}{\sigma} = \frac{a}{4}\left[\frac{2}{3}\theta_0 \frac{1-\mu^2+9\mu^4/4}{1+3\mu^2/4} + \lambda \frac{1-\mu^2}{1+3\mu^2/4}\right] \tag{19}$$

where a is the lift slope factor assumed to be 5.7. In Equation (19), σ is the *solidity* of the rotor defined as

$$\sigma = \frac{N_{\text{blades}} c}{\pi R} \tag{20}$$

With the collective θ_0, the flapping harmonics can be derived from the solution of the blade-flapping equation:

$$\beta_0 = \frac{\gamma}{8}\left[\theta_0(1+\mu^2) + \frac{4}{3}\lambda - \frac{4}{3}\mu\beta_{1c}^{(\text{nfp})}\right] \tag{21}$$

$$\beta_{1c}^{(\text{nfp})} = \frac{\mu(\frac{8}{3}\theta_0 + 2\lambda)}{1+\frac{3}{2}\mu^2} \tag{22}$$

$$\beta_{1s}^{(\mathrm{nfp})} = \frac{\frac{4}{3}\mu\beta_0}{1 + \frac{1}{2}\mu^2} \tag{23}$$

where the superscript (nfp) indicates that the flapping harmonics β_0, β_{1s} are relative to the *no-feathering plane*, while λ is relative to the tip-path plane. The definition of the no-feathering plane and the relation to the tip-path plane can be found in References [24, 25]. In Equation (21), γ is the *Lock number* defined as

$$\gamma = \frac{\rho a c R^4}{I} \tag{24}$$

where c is the blade chord and I the moment of inertia about the flap hinge. A typical value of $\gamma = 8.0$ is used here. The following assumptions are then made:

$$\beta_{1c} = \theta_{\mathrm{tpp}} - \theta_{\mathrm{shaft}} \tag{25}$$

$$\beta_{1s} = 0 \tag{26}$$

where θ_{shaft} is the tilt angle of the rotor. The assumption $\beta_{1s} = 0$ means that the tip-path plane is not tilted sideways. From the geometric relations between the tip-path plane and no-feathering plane, the cyclic harmonics required to obtain this state are

$$\theta_{1s} = \beta_{1c}^{(\mathrm{nfp})} - \beta_{1c} \tag{27}$$

$$\theta_{1c} = -\beta_{1s}^{(\mathrm{nfp})} + \beta_{1s} \tag{28}$$

The present trimming model neglects the lead-lag deflection of the blades, which has only a secondary effect on the rotor blade aerodynamics.

A hovering rotor, for which $\mu = 0$, represents the simplest trimming case. For this case, the collective pitch θ_0 and the coning angle β_0 of the rotor are unknowns. The procedure consists of the following steps:

1. At start-up, an initial estimate of the trim state is computed using the following equation for the collective pitch:

$$\theta_0 = \frac{6}{\sigma a} C_{\mathrm{T}} + \frac{3}{2}\sqrt{\frac{C_{\mathrm{T}}}{2}} \tag{29}$$

   In this case, the inflow factor λ can be obtained directly from the equation:

$$\lambda = -\sqrt{\frac{C_{\mathrm{T}}}{2}} = -\frac{\sigma a}{16}\left[\sqrt{1 + \frac{64}{3\sigma a}\theta_0} - 1\right] \tag{30}$$

   For a twisted rotor blade, Equation (29) gives the collective pitch at 0.75 of the rotor radius R. Equation (21) for the coning angle β_0 is then used:

$$\beta_0 = \frac{\gamma}{8}\left[\theta_0 + \frac{4}{3}\lambda\right] \tag{31}$$

2. The mesh is subsequently deformed to account for the new rotor blade incidence and position.

3. A steady flow simulation is performed until a prescribed level of convergence is reached.
4. After n_{retrim} steps, a re-trimming is performed. The collective is updated using the following relation:

$$\delta\theta_0 = \frac{C_{\text{T, target}} - C_{\text{T}}}{\mathrm{d}C_{\text{T}}/\mathrm{d}\theta_0} \tag{32}$$

$$\frac{\mathrm{d}C_{\text{T}}}{\mathrm{d}\theta_0} = \frac{\sigma a}{6}\left[1 - \frac{1}{\sqrt{1 + (64/3\sigma a)\theta_0}}\right]$$

   Equation (31) gives the coning angle for the new collective pitch $\theta_0 + \delta\theta_0$.
5. Steps 2–4 are repeated until a constant trim state is reached.

3. VALIDATION OF THE FRAMEWORK

Validation is now presented for each of the main components: the hover formulation, the forward flight method, the grid motion/deformation algorithm as well as the rotor trimming. Several rotor cases have been employed and the planform shapes of all computed rotors are given in Figure 4.

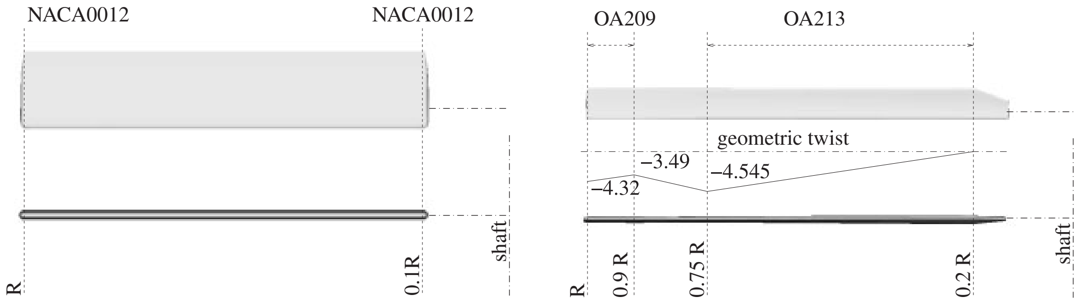

Caradonna & Tung rotor blade: Λ = 6.0

ONERA 7A rotor blade: Λ = 15.0

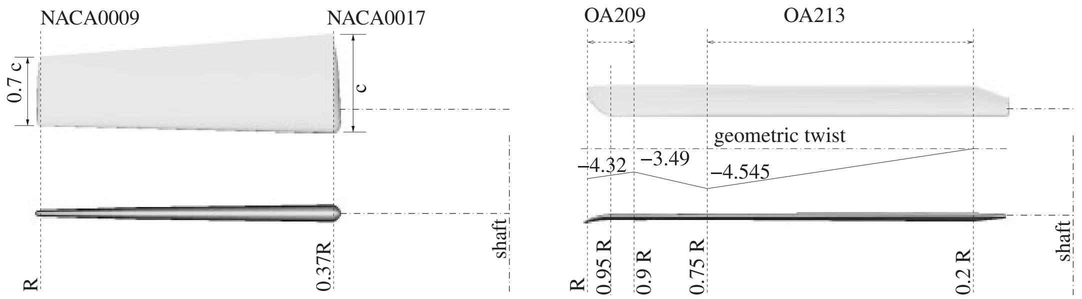

ONERA model rotor blade: Λ = 4.7

ONERA 7AD1 rotor blade: Λ = 15.0

Figure 4. Rotor blades employed for validation. Λ denotes the rotor aspect ratio (rotor radius over root chord).

3.1. Hovering rotors

The Caradonna and Tung [18] and the ONERA 7A/7AD1 rotors [19] have been used for the validation of the hover formulation. A summary of all hover cases is given in Table II. Computations for all test cases have been performed on full-rotor grids as well as blade-periodic ones. The test cases range from simple two-bladed, non-lifting rotors of simple planform, to lifting cases with high tip Mach number as well as four-bladed rotors of complex planform with an advanced blade tip with anhedral.

Caradonna and Tung [18] carried out an experimental and analytical study of a model helicopter rotor in hover. The experimental study involved simultaneous blade pressure measurements and tip vortex surveys. The rotor employed two cantilever-mounted, manually adjustable blades. The blades had a NACA 0012 profile and were untwisted and untapered. The rotor aspect ratio, defined as the ratio of rotor radius and blade chord was 6. The model rotor had a diameter of 2.286 m, and a chord length of 0.191 m. The experiments were carried out at various collective pitch settings and rotation rates. Collective settings θ_c from 0 to 12° and tip Mach numbers ranging from 0.23 to 0.9 were used. In the Caradonna–Tung experiment, the surface pressure distribution was measured at 5 rotor blade sections ($r/R = 0.50$, 0.68, 0.80, 0.89 and 0.96). The first test case was non-lifting at zero collective. Since the rotor was not generating lift, there was no induced downward velocity. As a result, this case converged faster than lifting cases and was less sensitive to the imposed boundary conditions at the upper and lower domain boundaries. Results are shown for two stations: $r/R = 0.80$ and 0.96. Figure 5 shows the comparison of the computed and measured wall pressure distributions. For this case the agreement between the results from the inviscid simulation and the experimental data is excellent. There is no difference in the results obtained using the periodic and the full meshes. Viscous results using the k–ω model are also presented and again good agreement has been obtained. For this case, grids with fine near-wall resolutions were needed (10^{-5} of blade chord), however, the same multi-block topologies are applicable.

The same radial stations have been used for the lifting case. Figures 6(a) and (b) show the comparison of the computed surface pressure distribution on the full rotor mesh with the measured data for $r/R = 0.80$ and 0.96, respectively. For the periodic mesh, Figures 6(c) and (d) present the same comparison. The figures show very good agreement between the

Table II. Summary of conditions for hovering Caradonna–Tung (C–T) and ONERA 7A/7AD1 rotors.

	C–T	C–T	7A	7AD1
Flow conditions				
Tip Mach number, M_{tip}	0.520	0.439	0.6612	0.6612
Reynolds number	2.3×10^6	1.9×10^6	2.1×10^6	2.1×10^6
Collective pitch, θ_c	0°	8°	$\theta_{0.7} = 7.5°$	$\theta_{0.7} = 7.5°$
Computation details				
Grid size (full rotor)	2 200 000	4 000 000	2 400 000	—
Grid size (periodic)	1 100 000	2 000 000	600 000	600 000 and 1 300 000
Modelling	Inviscid/ k–ω	Inviscid/ k–ω	Inviscid	Inviscid

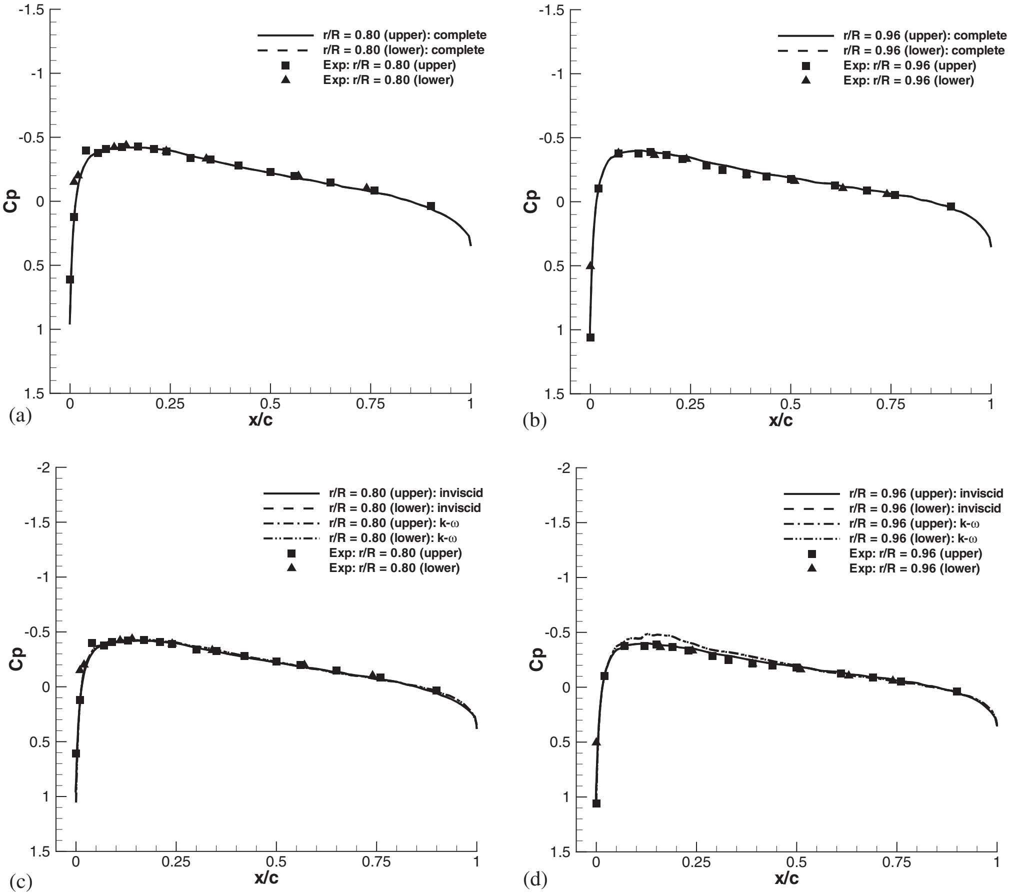

Figure 5. C_p comparison for the Caradonna and Tung non-lifting case: $\theta_c = 0°$, $M_{\text{tip}} = 0.520$: (a) $r/R = 0.96$ (full mesh); (b) $r/R = 0.987$ (full mesh); (c) $r/R = 0.826$ (periodic mesh); and (d) $r/R = 0.987$ (periodic mesh).

computed and measured surface pressure distributions. As for the non-lifting case, there is no difference between the results obtained on the full and the periodic meshes. A slightly better prediction of the suction peak (Figures 6(c) and (d)) has been obtained for the viscous results.

The 7A/7AD1 model rotors were tested in the DNW wind tunnel during the HELISHAPE research campaign [19]. These are four-bladed rotors with 2.1 m radius, 0.14 m chord and have a non-constant geometric twist. The rotors have a rectangular planform and consist of ONERA OA213 and OA209 aerofoil sections. The rotor blade aspect ratio is 15. Figure 4 summarizes the geometrical data for the rotors. Results are shown for a collective pitch setting 7.5° at $r/R = 0.7$. The required CPU time for a representative 7A hover simulation is given in Table V. Figures 7(a) and (b) show the comparison of the computed surface pressure distribution on the full rotor mesh with the measured data for $r/R = 0.826$ and 0.987,

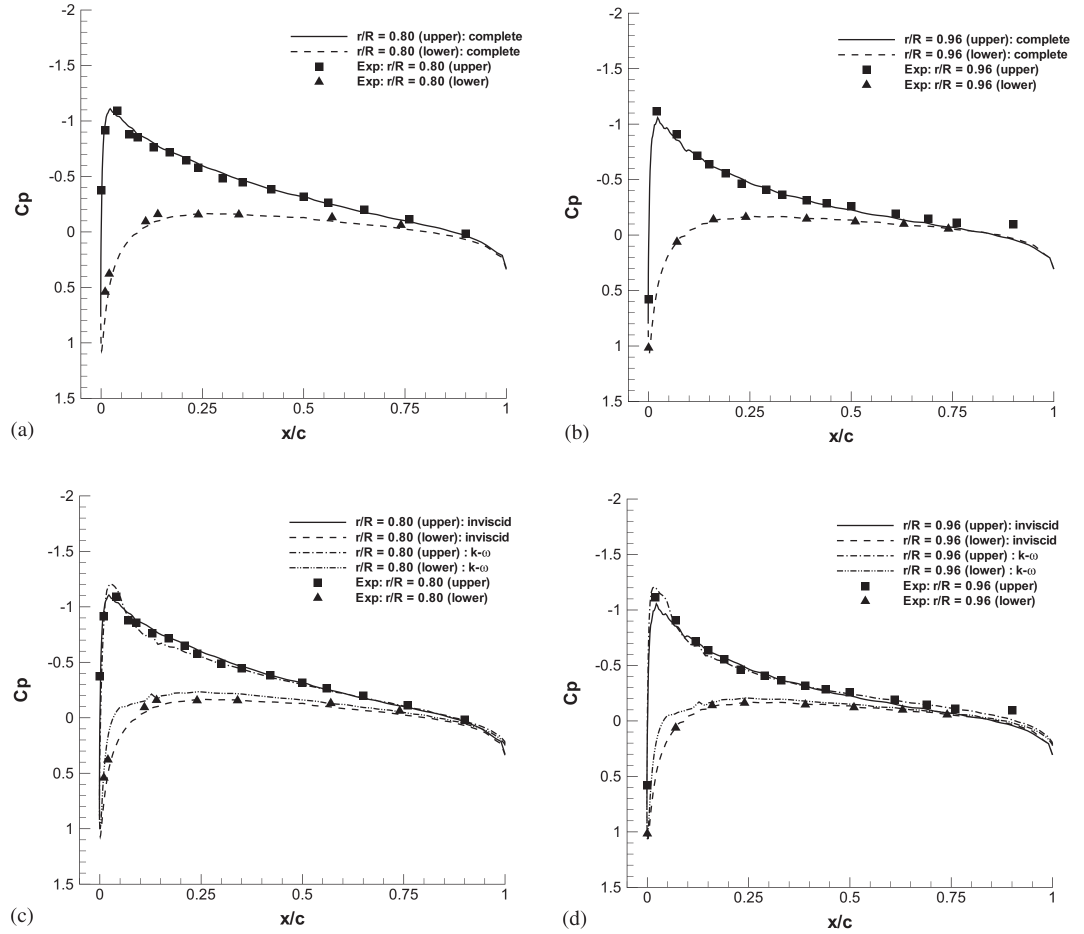

Figure 6. C_p comparison for the Caradonna and Tung lifting case: $\theta_c = 8°$ and $M_{\text{tip}} = 0.439$: (a) $r/R = 0.80$ (full grid); (b) $r/R = 0.96$ (full grid); (c) $r/R = 0.80$ (periodic mesh); and (d) $r/R = 0.96$ (periodic mesh).

respectively. For the periodic mesh, Figures 7(c) and (d) present the same comparison. The experimental data reported in Reference [28] were used. As with the simulations for the Caradonna–Tung test case, there is excellent agreement between the results on the full and periodic grids.

Similar conclusions can be drawn from the results obtained for the ONERA 7AD1 rotor. This case has a complex parabolic tip with anhedral in addition to a non-constant geometric twist distribution, similar to the one of the 7A rotor. For this case results in Figure 8 are only presented for computations on periodic grids. Since this is the hardest hover case considered in this paper, results are shown for two different grids and at four spanwise stations. The agreement between experiments and simulation remains excellent for all four stations and there is no significant difference between the results obtained on the two grids, the finer

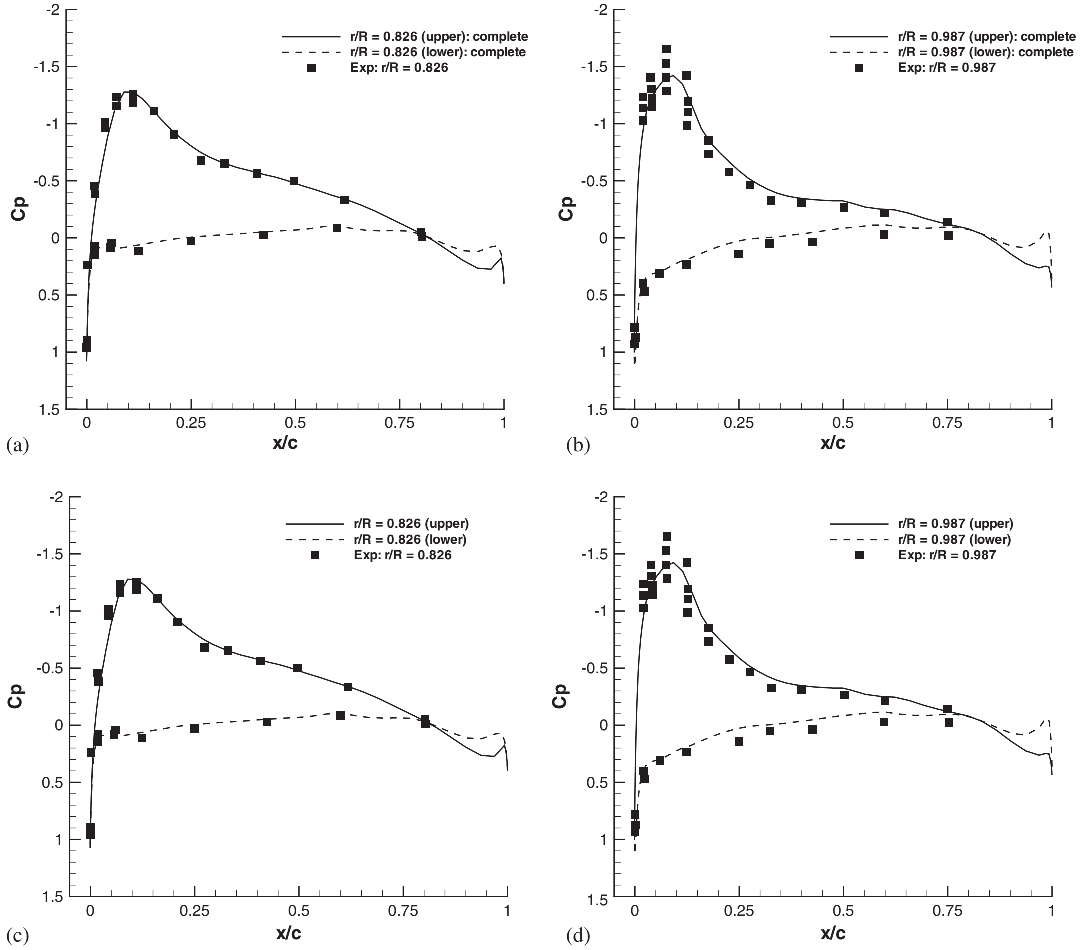

Figure 7. C_p comparison for the ONERA 7A hovering rotor. $M_{\text{tip}} = 0.6612$: (a) $r/R = 0.826$ (full mesh); (b) $r/R = 0.987$ (full mesh); (c) $r/R = 0.826$ (periodic mesh); and (d) $r/R = 0.987$ (periodic mesh).

of which includes 1.3 million points. In addition, the 7AD1 hover test case demonstrates that the blocking strategy described in Section 2.6 can be used with complex parabolic tip shapes.

3.2. *Forward flight cases*

Two cases have been considered for validation of the forward flight formulation. The details of the cases in terms of the employed blade actuations and flow conditions are given in Table III. The first test case is for a non-lifting rotor for which experimental data is available for the surface pressure on the advancing side. This test case models a rotor in high-speed forward flight and numerical results are compared against experimental data for the surface pressure on the advancing side. A second test case considers a two-bladed lifting rotor in forward flight

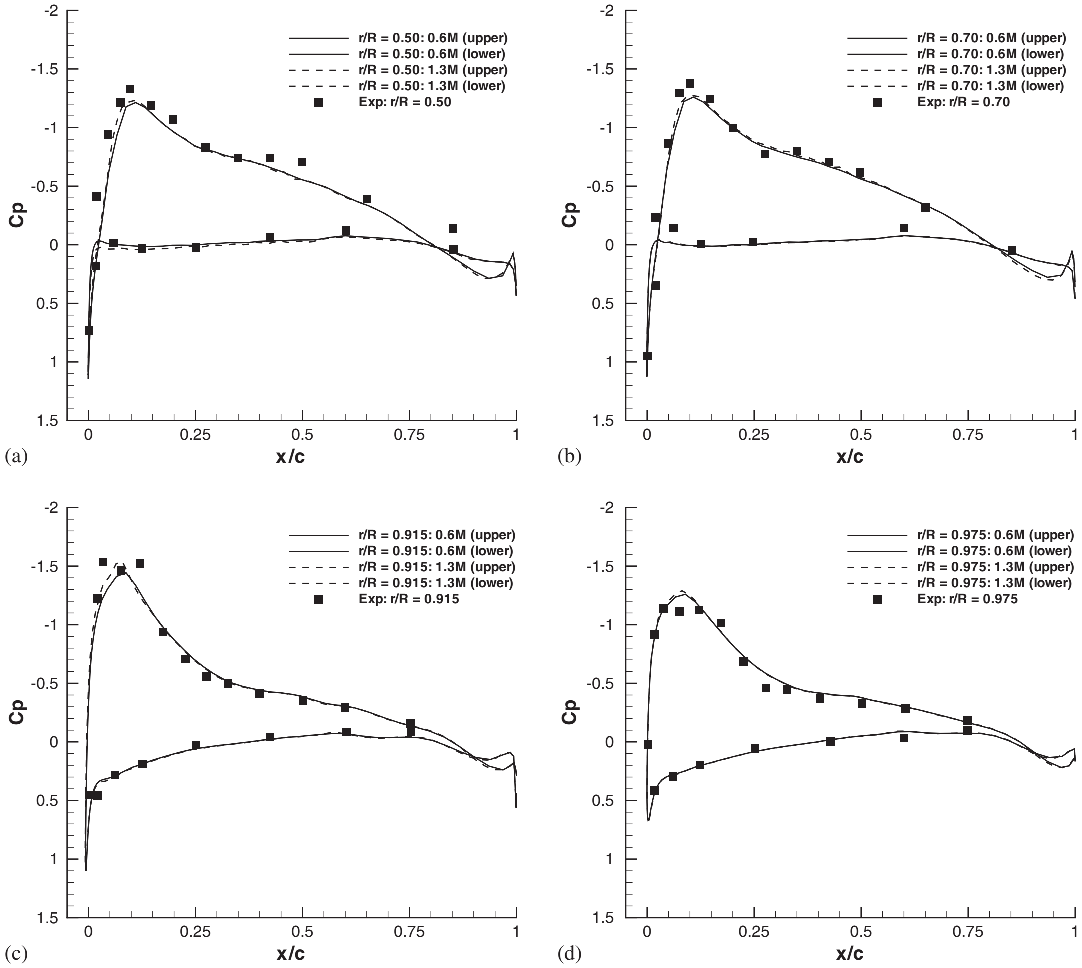

Figure 8. C_p comparison for the ONERA 7AD1 hovering rotor. $M_{\text{tip}} = 0.6612$: (a) $r/R = 0.5$; (b) $r/R = 0.7$; (c) $r/R = 0.915$; and (d) $r/R = 0.975$, solutions have been obtained on a periodic grid.

Table III. Summary of conditions for forward flight test cases.

Case	M_{tip}	μ	θ_0	θ_{1s}	θ_{1c}	β_0	β_{1s}	β_{1c}	δ_0	δ_{1s}	δ_{1c}
1	0.625	0.5	0°	0°	0°	0°	0°	0°	0°	0°	0°
2	0.60	0.25	4.0°	2.0°	0.0°	1.5°	2.0°	2.0°	0.0°	–2.0°	0.0°

with prescribed harmonic pitch changes, flapping and lead-lag deflections thus demonstrating the capability of the present method to simulate a fully articulated rotor in forward flight.

3.2.1. ONERA two-bladed model rotor. This test case involves the non-lifting forward flight of a two-bladed model rotor, tested at ONERA [20]. The rotor had untwisted blades with symmetric profiles of the NACA four-digit family, a radius of $R = 0.75$ m and a trapezoidal planform ($c = 0.166$m at $0.37R$ and 0.115m at the tip). The profile relative thickness decreased linearly from 17% at the root to 9% at the tip. For the test case studied here, the forward flight Mach number was 0.3125 and the tip Mach number was 0.625 giving an advance ratio of 0.50. Experimental data is available for four azimuthal positions $\psi = 30, 60, 90$ and 120° and for two radial stations $r/R = 0.85$ and 0.90. Since this is a non-lifting case, it can only be used as a first validation step of the forward flight formulation. The required CPU time for this test case is given in Table V. For the radial station $r/R = 0.85$, the chord-wise surface pressure coefficient is plotted versus the azimuthal position ψ in Figure 10 for the advancing side of the rotor. Here, the C_p is based on the local blade-normal Mach number. At $\psi = 0°$ the local blade normal Mach number at $r/R = 0.85$ is 0.531 and a shock-free pressure distribution can be seen. As the azimuth increases to 90°, the local blade normal Mach number increases. From about $\psi = 60°$, a local supersonic region forms closed by a shock. From $\psi = 90°$, the local blade normal Mach number decreases and the shock wave vanishes at $\psi = 160°$. A marked asymmetry can be observed for the shock wave location, i.e. the pressure distributions for $\psi = 60$ and 120° (for which the blade normal Mach number is identical) are quite different. For the radial stations $r/R = 0.85$ and 0.90, the computed surface pressure coefficient is compared to the experimental data in Figure 9. Numerical results for two different meshes are shown. Both meshes had a C–H topology around the blades and 236 grid blocks, the densities for the coarse and fine grids were 1.2×10^6 and 1.8×10^6 points, respectively. A step size in azimuth of 0.25° has been used. The agreement with the experimental data was very good for both meshes with the finer grid producing, as expected, a slightly stronger suction peak at $\psi = 150°$. The main challenge in this case was to capture the highly dynamic shock formation and decay process, which can be seen in Figure 10. The asymmetry of the pressure distribution shown in Figure 10 can also be seen in Figure 9. For the retreating side, no experimental data was available. The obtained results are, however, more than encouraging.

3.2.2. Articulated rotor in forward flight. This test case involves the lifting forward flight of a two-bladed rotor. The rotor blades are untapered, untwisted with an aspect ratio of 6. The blades are made of NACA0012 profiles. Table III summarizes the input data for the test case. The required CPU time for this test case is given in Table V. Figure 11 presents the loading of the rotor disk along with sectional distributions of the surface pressure coefficient at various azimuth angles. On the same figure the incidence is given as a function of the azimuth. It is evident that on the advancing side the contributions of pitching and flapping result in a significant reduction of the incidence and this is reflected in the loading of the rotor. Figure 11 suggests that between 70 and 150° of azimuth only a small amount of lift is produced on the advancing side. On the retreating side, the incidence plot indicates an increase of incidence due to the pitching and flapping harmonics. Consequently, the sectional C_p distributions indicate significant amounts of lift. The location of the blades relative to the disk plane is also shown. The blue shade on the figure corresponds to the location of the blade at constant collective and coning angles, while the grey shade indicates the instantaneous position of the blade. The overall loading of the rotor disk highlights the lack of a trimmed state for this case and clearly shows that the rear of the disk is much more loaded than the front part.

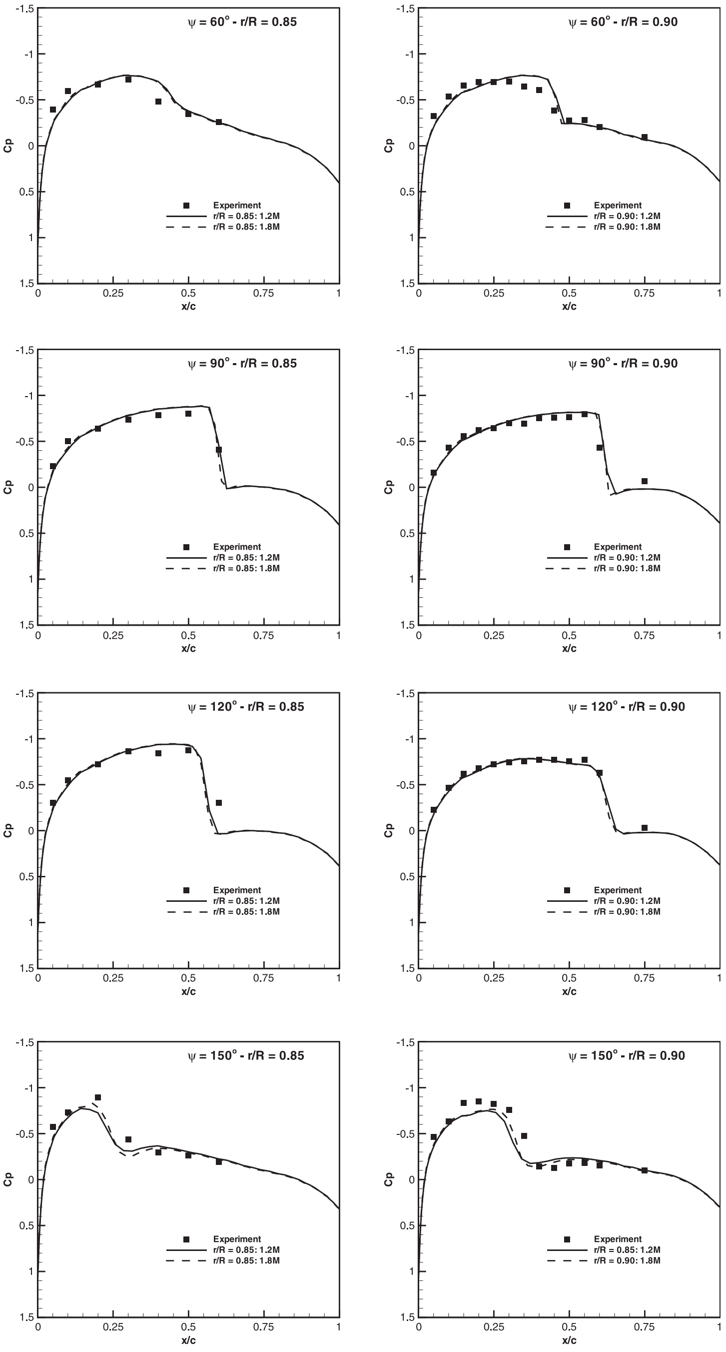

Figure 9. Chord-wise C_p distributions for the ONERA two-bladed model rotor at two radial stations ($r/R = 0.85$ and 0.90) for $M_{\text{tip}} = 0.625$ and advance ratio $\mu = 0.50$.

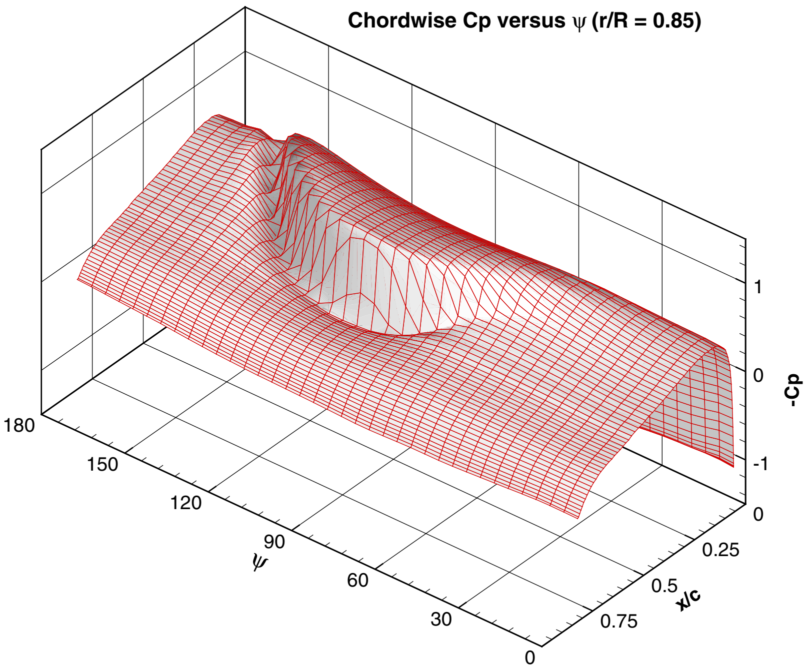

Figure 10. Chord-wise C_p for ONERA two-bladed model rotor in forward flight for $0^\circ \leqslant \psi \leqslant 180^\circ$ $(r/R = 0.85)$.

Table IV. Computed revolution-averaged thrust and moment coefficients for the fully articulated, forward-flying rotor.

	C_z	$C_{m,x}$	$C_{m,y}$
Rev. 2	0.003511	−0.000568	−0.000355
Rev. 3	0.003551	−0.000569	−0.000333

Using the surface pressure at each azimuth, the revolution-averaged thrust and moments were computed. For the second and third revolution of the rotor, non-dimensionalised, averaged loads and moments are shown in Table IV. Comparing the values for the second and third revolution, a good level of convergence can be demonstrated. In Table IV, C_z is the thrust of the rotor (positive upward), $C_{m,x}$ the roll moment and $C_{m,y}$ the pitching moment of the rotor. The following non-dimensionalizations are used:

$$C_z = \frac{F_z}{\pi R^2 \rho v_{\text{tip}}^2}, \quad C_{m,x} = \frac{M_x}{\pi R^3 \rho v_{\text{tip}}^2}, \quad C_{m,y} = \frac{M_y}{\pi R^3 \rho v_{\text{tip}}^2}$$

The non-zero values of $C_{m,x}$ and $C_{m,y}$ clearly show that the rotor is not in a trimmed state (Table V).

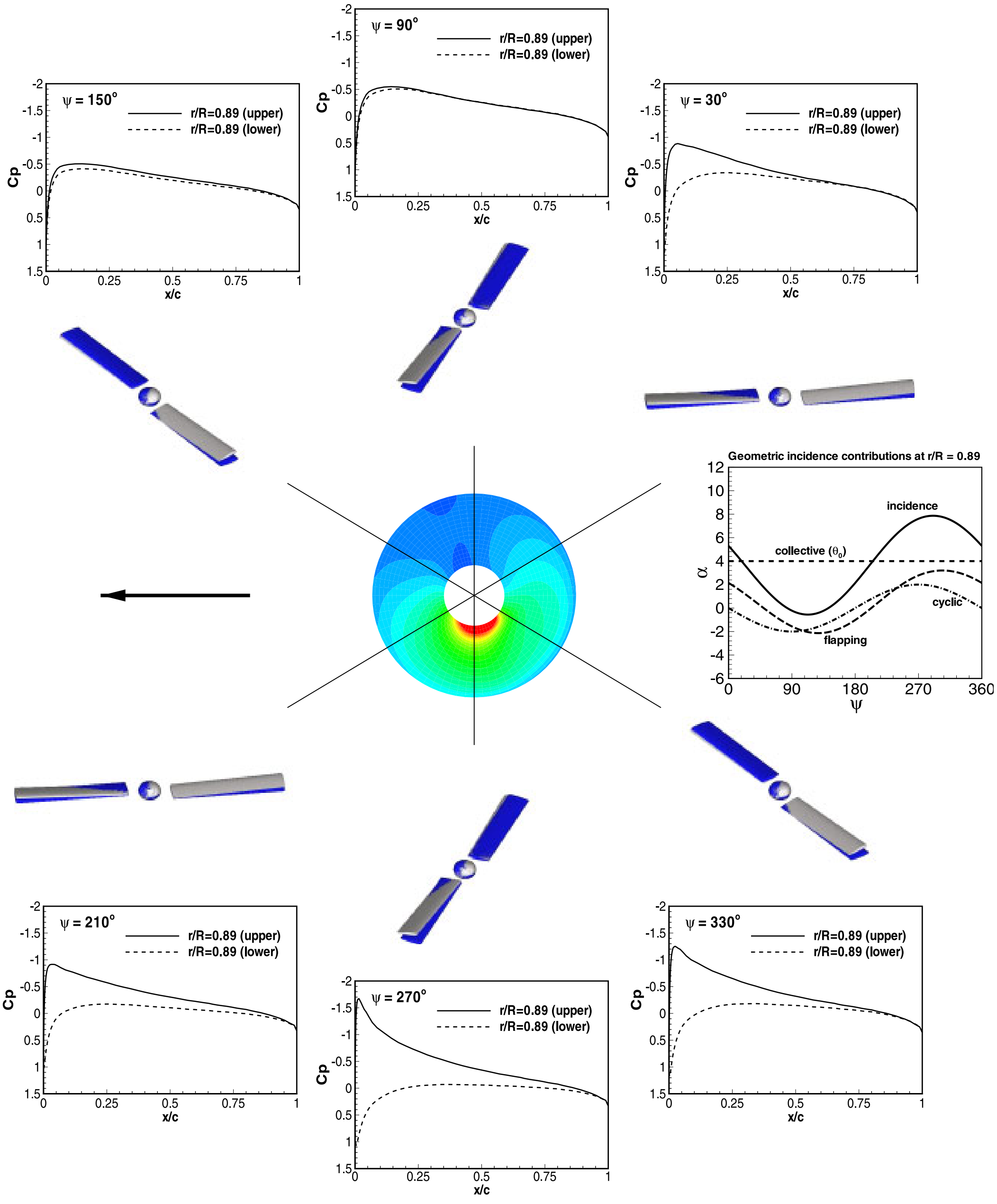

Figure 11. Two-bladed articulated rotor in forward flight. The surface pressure distribution is shown at six azimuth angles along with the variation of the incidence. The rotor disk loading is shown at the centre. ($M_{\text{tip}} = 0.60$, $\mu = 0.25$, sectional C_p distributions at $r/R = 0.89$.).

Table V. CPU requirements for rotor computations (all results obtained on Pentium 4 processors).

Type Rotor	Hover untrimmed 7A	Hover trimmed 7A	Forward-flight non-lifting ONERA model	Forward-flight articulated Two-bladed model
# revolutions	—	—	3	3
Mesh size	600 000	600 000	1 200 000	1 200 000
# procs.	8	8	18	18
CPU time (h)	2	3	72	72

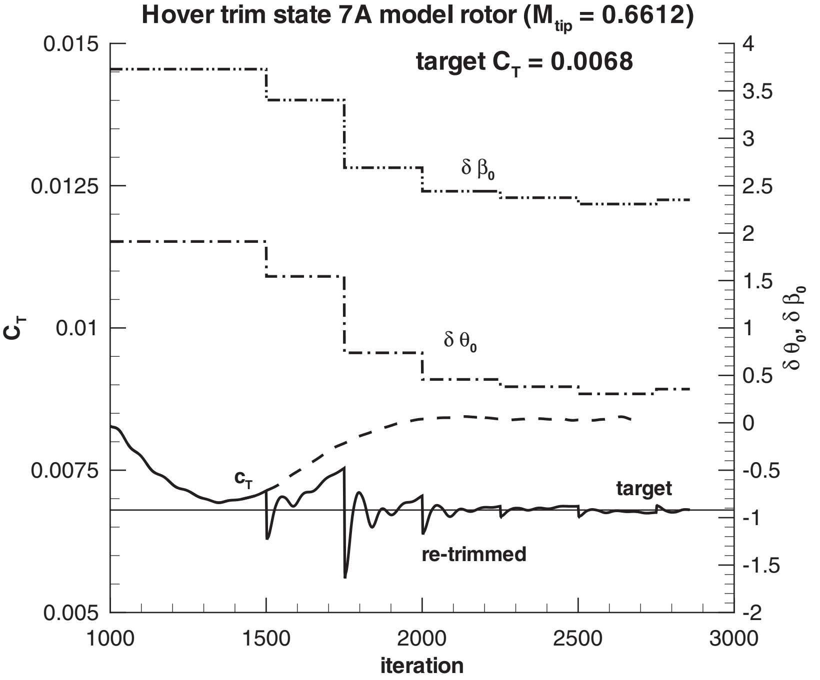

Figure 12. Simulation of hover trim-state for 7A model rotor: $M_{\text{tip}} = 0.6612$, target $C_T = 0.0068$.

3.3. Trimmed rotor cases

Figures 12 and 13 show sample results for the ONERA 7A model rotor in hover. The figures compare results based on the initial trim approximation and results obtained using a re-trimming after every 250 iterations. The employed grid had a built-in collective pitch of 7.5° at 70% of the rotor radius and 0° of coning. Figure 12 presents the results for a target $C_T = 0.0068$ and tip Mach number 0.6612. The initial trimming over-predicts the collective pitch and without subsequent re-trimming the solution converges to a C_T value above 0.0068. The re-trimming leads to a step reduction in the collective pitch, until converging to a value 0.35° larger than the built-in collective pitch. The final C_T matches the target value. The coning angle converges to a value of 2.3°. Figure 13 shows results for a target $C_T = 0.0050$, which required a reduction of the collective pitch relative to the built-in collective pitch.

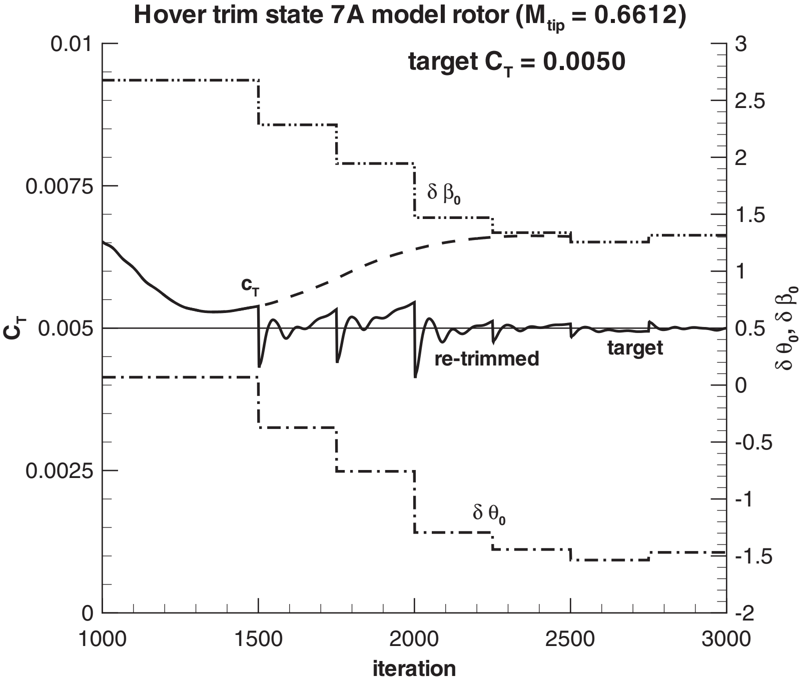

Figure 13. Simulation of hover trim-state for 7A model rotor: $M_{\mathrm{tip}} = 0.6612$, target $C_{\mathrm{T}} = 0.0050$.

Table VI. Results from trim-state calculations for ONERA 7A model rotor, $M_{\mathrm{tip}} = 0.6612$, re-trimming every 250 pseudo-time steps.

$C_{\mathrm{T,target}}$	Initial	retrim 1	retrim 2	retrim 3	retrim 4	retrim 5	retrim 6
0.0000	$\theta_0 = 0.00$	0.54	−0.53	−0.58	−0.59	−0.60	−0.61
(re-trim)	$\beta_0 = 0.00$	0.00	0.00	0.00	0.00	0.00	0.00
0.0050	$\theta_0 = 7.57$	7.13	6.74	6.21	6.06	5.97	6.02
(re-trim)	$\beta_0 = 2.68$	2.29	1.95	1.47	1.34	1.26	1.31
0.0068	$\theta_0 = 9.41$	9.04	8.24	7.95	7.88	7.80	7.85
(re-trim)	$\beta_0 = 3.73$	3.40	2.69	2.44	2.37	2.31	2.35
0.0085	$\theta_0 = 11.07$	11.14	9.90	9.70	9.64	9.63	9.62
(re-trim)	$\beta_0 = 4.71$	4.77	3.68	3.51	3.46	3.44	3.44

Again, the result without re-trimming over-predicted the C_{T} value and the simulation with re-trimming converged to the specified target. The collective at convergence was 1.5° lower than the built-in collective pitch, while the coning angle converged to a value of 1.3°. The details of several cases computed for this work are given in Table VI. For the first example of Table VI a target thrust coefficient of zero was requested and a fixed coning angle of zero degrees has been imposed. The final collective angle of −0.61° corresponds to the zero-lift incidence of this rotor. This is an interesting case since it highlights the combined effect of the cambered sections and the non-linear geometric twist used for the ONERA 7A rotor. It is also evident that both collective and coning increase with the thrust coefficient and this result in a considerable increase of the required power. The dashed line in Figures 12 and 13 shows the convergence of the thrust coefficient without any trimming. As can be seen, the overhead of the present trimming algorithm in comparison to a hover calculation without trimming at a given set of collective and coning angles is moderate. Figures 12 and 13 indicate that an increase between 50 and 70% of the number of iterations is required. The CPU times for representative trimmed 7A hover computations are given in Table V.

4. CONCLUSIONS

A CFD framework has been presented and validated which allows the efficient and accurate computation of helicopter rotor flows. Key ingredients are: (i) the time-dependent Reynolds-averaged Navier–Stokes equations which permit for non-linear, unsteady aerodynamic phenomena to be captured, (ii) the hover formulation which can simplify computations by transforming an unsteady problem to a steady-state one, (iii) a novel grid-deformation strategy that allows all blade motions to be taken into account separately and preserves the quality of the CFD grids, and finally, (iv) a simple trimming algorithm that allows computations to be performed for standard non-maneuvering rotor conditions. Results have been obtained for hovering and forward-flying rotors and comparisons against experimental data are encouraging. The validation cases covered a wide range of Mach numbers and angles, and for all cases the proposed method resulted in high-quality grids and efficient CPU times.

The superiority of the proposed treatment for the moving blades was demonstrated and high-quality grids were obtained both in the near- and far-field of the domain. In contrast, the TFI method resulted in highly skewed cells near the blade especially in the vicinity of the leading edge at moderate-to-high pitch angles. Blade flapping was also found to affect the grid quality near the tip. Again, the current method provided a solution with grids of high quality able to capture the blade loading.

This work is part of a wider effort undertaken by the authors in predicting unsteady rotor flows. Separate from validation efforts, future research is now directed towards the coupled rotor/fuselage problem. In addition, the periodic nature of the flow is to be exploited for the efficient computation of rotor flows. These results will be reported in future papers.

ACKNOWLEDGEMENTS

The financial support of the Engineering Physical Sciences Research Council (EPSRC) and the U.K. Ministry of Defence (MoD) under the Joint Grant Scheme is gratefully acknowledged for this project. This work forms part of the Rotorcraft Aeromechanics Defence and Aerospace Research Partnership (DARP) funded jointly by EPSRC, MoD, DTI, QinetiQ and Westland Helicopters.

REFERENCES

1. Badcock K, Richards B, Woodgate M. Elements of computational fluid dynamics on block structured grids using implicit solvers. *Progress in Aerospace Sciences* 2000; **36**(5–6):351–392.
2. Biava M, Vigevano L. The effect of far-field boundary conditions on tip vortex path predictions in hovering. *CEAS Aerospace Aerodynamics Research Conference*, Cambridge, 10–13 June, 2002.

3. Renzoni R, D'Alascio A, Kroll N, Peshkin D, Hounjet M, Boniface J-C, Vigevano L, Morino L, Allen CB, Badcock KJ, Mottura L, Scholl M, Kokkalis E. A common European Euler code for the analysis of the helicopter rotor flowfield. *Progress in Aerospace Sciences* 2000; **36**:437–485.
4. Altmikus ARM, Wagner S, Beaumier P, Servera G. A comparison: weak versus strong modular coupling for trimmed aeroelastic rotor simulations. *American Helicopter Society 58th Annual Forum*, Montreal, Quebec, June 2002.
5. Pahlke K, van der Wall B. Calculation of multibladed rotors in high-speed forward flight with weak fluid–structure-coupling. *27th European Rotorcraft Forum*, Moscow, Russia, September 2001.
6. Pomin H, Wagner S. Navier–Stokes analysis of helicopter rotor aerodynamics in hover and forward flight. *Journal of Aircraft* 2002; **39**(5):813–821.
7. Pomin H, Wagner S. Aeroelastic analysis of helicopter rotor blades on deformable chimera grids. *Journal of Aircraft* 2004; **41**(3):577–584.
8. Servera G, Beaumier P, Costes M. A weak coupling method between the dynamics code HOST and the 3D unsteady Euler code WAVES. *Aerospace Science and Technology* 2001; **5**:397–408.
9. Park Y, Kwon O. Simulation of unsteady rotor flow field using unstructured adaptive sliding meshes. *Journal of the American Helicopter Society* 2004; **49**(4):391–400.
10. Chen CL, McCroskey WJ, Obayashi S. Numerical solutions of forward-flight rotor flow using an upwind method. *Journal of Aircraft* 1991; **28**(6):374–380.
11. Srinivasan GR, Baeder JD. TURNS: a free-wake Euler–Navier–Stokes numerical method for helicopter. *AIAA Journal* 1993; **31**(5):959–962.
12. Rouzaud O, Raddatz J, Boniface JC. Euler calculations of multibladed rotors in hover by DLR and ONERA methods and comparison with helishape tests. *American Helicopter Society 53rd Annual Forum*, Virginia Beach, 29 April–1 May 1997.
13. Potsdam M, Yeo W, Johnson W. Rotor airloads prediction using loose aerodynamic/structural coupling. *American Helicopter Society 60th Annual Forum*, Baltimore, MD, 7–10 June 2004.
14. Allen CB. An unsteady multiblock multigrid scheme for lifting forward flight rotor simulation. *International Journal for Numerical Methods in Fluids* 2004; **45**(9):943–984.
15. Conlisk AT. Modern helicopter aerodynamics. *Annual Review of Fluid Mechanics* 1997; **29**:515–567.
16. Boelens OJ, van der Ven H, Oskam B, Hassan AA. Boundary conforming discontinuous Galerkin finite element approach for rotorcraft simulations. *Journal of Aircraft* 2002; **39**(5):776–785.
17. Van der Ven H, Boelens OJ. A framework for aeroealistic simulations of trimmed rotor systems in forward flight. *European Rotorcraft Forum*, Marseille, September 14–16, 2004.
18. Caradonna FX, Tung C. Experimental and analytical studies of a model helicopter rotor in hover. *Technical Report*, *NASA Technical Memorandum 81232*, 1981.
19. Schultz KJ, Splettstösser W, Junker B, Wagner W, Arnaud G *et al.* A parametric windtunnel test on rotorcraft aerodynamics and aeroacoustics (helishape)—test procedures and representative results. *Aeronautical Journal* 1997; **101**(1004):143–154.
20. Philippe J-J, Chattot J-J. Experimental and theoretical studies on helicopter blade tips at ONERA. *Sixth European Rotorcraft and Powered Lift Aircraft Forum*, Bristol, 16–19 September 1980.
21. Osher S, Chakravarthy S. Upwind schemes and boundary conditions with applications to Euler equations in general geometries. *Journal of Computational Physics* 1983; **50**:447–481.
22. Jameson A. Time dependent calculations using multigrid, with applications to unsteady flows past airfoils and wings. *AIAA Paper 91-1596*, 1991.
23. Axelsson O. *Iterative Solution Methods*. Cambridge University Press: Cambridge, MA, 1994.
24. Bramwell ARS. *Helicopter Dynamics* (1st edn). Edward Arnold: London, 1976.
25. Seddon J. *Basic Helicopter Aerodynamics* (1st edn). BSP Professional Books: Oxford, 1990.
26. Newman S. *The Foundations of Helicopter Flight*. Arnold: London, 1994.
27. Nikolsky AA. *Helicopter Analysis*. Wiley: New York, 1951.
28. European Community Industrial & Materials Technologies Programme (Brite-Euram III). Development of a Common European Euler Code for Helicopter Rotors (EROS). Project: BE95-1373, November 1999.